Surface & Coatings Technology 477 (2024) 130326

Contents lists available at ScienceDirect

Surface & Coatings Technology

journal homepage: www.elsevier.com/locate/surfcoat

Elemental distribution and fracture properties of magnetron sputtered carbon supersaturated tungsten films

S. Fritze [a,*], R. Hahn [b], H. Aboulfadl [c], F.O.L. Johansson [d,e,f], R. Lindblad [a], K. Böőr [a], A. Lindblad [g], E. Berggren [g], D. Kühn [e], T. Leitner [e], B. Osinger [a], E. Lewin [a], U. Jansson [a], P.H. Mayrhofer [b], M. Thuvander [c]

[a] Department of Chemistry-Ångström, Uppsala University, Box 538, SE-75121 Uppsala, Sweden
[b] Institute of Materials Science and Technology, TU Wien, A-1060 Vienna, Austria
[c] Department of Physics, Chalmers University of Technology, SE-412 96 Göteborg, Sweden
[d] Division of Applied Physical Chemistry, Department of Chemistry, KTH – Royal Institute of Technology, SE-100 44 Stockholm, Sweden
[e] Institute Methods and Instrumentation for Synchrotron Radiation Research PS-ISRR, Helmholtz-Zentrum Berlin für Materialien und Energie, Albert-Einstein-Straße 15, 12489 Berlin, Germany
[f] Institut für Physik und Astronomie, Universität Potsdam, Karl-Liebknecht-Strasse 24-25, 14476 Potsdam, Germany
[g] Division of X-ray Photon Science, Department of Physics and Astronomy, Uppsala University, Box 516, 751 20 Uppsala, Sweden

ARTICLE INFO

Keywords:
PVD
Fracture toughness
Atom probe tomography
XPS
Tungsten

ABSTRACT

The combination of strength and toughness is a major driving force for alloy design of protective coatings, and nanocrystalline tungsten (W)-alloys have shown to be promising candidates for combining strength and toughness. Here we investigate the elemental distribution and the fracture toughness of carbon (C) alloyed W thin films prepared by non-reactive magnetron sputtering. W:C films with up to ~4 at.% C crystallize in a body-centered-cubic structure with a strong ⟨hh0⟩texture, and no additional carbide phases are observed in the diffraction pattern. Atom probe tomography and X-ray photoelectron spectroscopy confirmed the formation of such a supersaturated solid solution. The pure W film has a hardness ~13 GPa and the W:C films exhibit a peak hardness of ~24 GPa. In-situ micromechanical cantilever bending tests show that the fracture toughness decreases from ~4.5 MPa·$m^{1/2}$ for the W film to ~3.1 MPa·$m^{1/2}$ for W:C films. The results show that C can significantly enhance the hardness of W thin films while retaining a high fracture toughness.

1. Introduction

Materials properties can often be enhanced by reducing the grain size [1], and magnetron sputtering is a well-established technique to synthesize nanocrystalline (nc) materials. Nc-tungsten (W) thin films often exhibit nanoindentation hardness values above 10 GPa [2], which is more than twice as high as single crystal W (~4 GPa) [3]. The high hardness values for nc-W are explained by the fact that W possesses a large Hall-Petch coefficient [3]. The properties of W are not only dependent on the microstructure but are also influenced by p-block impurities (< 1 at.%), which can be incorporated into the material during production [4,5]. These p-block impurities show a strong tendency to segregate towards the grain boundaries (GBs) upon heat treatment [5,6]. Tian et al. [5] reported that the phosphorous (P) content at the GBs increased from 0.07 at.% for an as-received W sample to 2.5 at.% for a recrystallized W sample. Additional fracture toughness measurements revealed that the increased P content at the GBs led to a significant loss of toughness [5]. Wurmshuber et al. [6] showed that boron (B) segregations to W GBs have a positive effect on the mechanical properties. They also report formation of W_2C grains when attempting to synthesize a W—C solid solution by means of high pressure torsion. First principle calculations by Scheiber et al. [7] suggest that B and carbon (C) have a positive effect on the cohesive strength of W GBs, while nitrogen (N) has no effect and oxygen (O) has a negative effect. These results suggest that it can be beneficial to synthesize materials supersaturated with B or C, which potentially segregate faster than O or P in the GBs, and thus enhance the cohesive strength of the GBs. Such materials have recently been synthesized by magnetron sputtering, where the high quenching rates suppress the formation of the equilibrium phases [8–11]. Yang et al. showed that the addition of ~6 at.% C or B to W led

* Corresponding author.
E-mail addresses: ist.stefanf@gmail.com (S. Fritze), barbara.osinger@kemi.uu.se (B. Osinger).

https://doi.org/10.1016/j.surfcoat.2023.130326
Received 25 July 2023; Received in revised form 11 November 2023; Accepted 17 December 2023
Available online 21 December 2023

to the formation of supersaturated body-centered cubic (bcc) W films that exhibit hardness values of ~25 GPa, almost twice as high as the ones from pure nc-W films. Furthermore, cube corner fracture toughness tests revealed that the films possessed a unique combination of metallic toughness and ceramic hardness [9–11]. Alternatively, other measurement methods can be used, where the residual stresses are released during the sample preparation. Soler et al. [12] showed that residual stresses significantly impact the toughness values obtained by indentation-based techniques and suggest that the measured toughness should be considered a system (film/substrate) property.

We have recently studied the effect of ~2 at.% and ~4 at.% C on the microstructure and the mechanical properties of bcc W films. X-ray diffraction (XRD) analysis showed that the lattice parameter increases with increasing C content and thus suggested that C occupies the octahedral positions of the W lattice [13,14]. Adding C reduced the column width from ~130 nm for W (with the columns consisting of a few grains) to ~20 nm (with the columns consisting of several grains) for the film containing ~4 at.% C, explained by a mechanism where C acts as renucleation sites. Micropillar compression tests showed that the flow stress increased upon C addition, from ~3.8 to ~8.3 GPa, and no brittle facture under compression was observed. The significant increase in hardness was explained by a combination of grain refinement strengthening, solid-solution strengthening, and an increased dislocation density [13].

This study aims to investigate if C is indeed homogeneously distributed in the magnetron sputtered W:C films, and if C affects the intrinsic toughness of the W:C films. Synchrotron X-ray photoelectron spectroscopy (XPS) was used to evaluate the local chemical environment of C atoms. Atom probe tomography (APT) was carried out to evaluate the distribution of C at the nanometer scale since APT is a well-established method for quantifying local compositions in three dimensions and segregations to interfaces with a high chemical sensitivity [15]. Microcantilever bending tests were used to evaluate the intrinsic toughness of free-standing coatings.

2. Methods

2.1. Film synthesis

A Qprep500i (Mantis Deposition Ltd.) ultra-high vacuum system was used to deposit W—C films by non-reactive direct current (DC) magnetron sputtering from elemental targets. The films in the present study, on 0.5 mm thick single crystal Si (001) substrates, were synthesized as part of the study in ref. [13]. The substrate temperature was ~300 °C and the deposition rate was ~600 nm/h. The overall film thickness was ~4.5 μm. A detailed description of the deposition process can be found in ref. [13].

2.2. Structural and chemical analysis

Grazing incidence and theta-2theta XRD (GI-XRD, θ/2θ) patterns were recorded using a Siemens D5000 diffractometer operated with a Cu-Kα source in parallel beam geometry.

Needle-shaped specimens for APT were prepared using a dual beam focused ion-beam/scanning electron microscopy (FIB/SEM) workstation (FEI™ Versa 3D). The specimen preparation was performed using the standard lift-out technique [16]. The APT measurements were performed in a LEAP 3000× HR IMAGO™ instrument in voltage pulse mode with a specimen base temperature of ~60 K, pulse fraction of 20 %, and a repetition rate of 200 kHz. The commercial software IVAS 3.6 was used to reconstruct and analyze the APT data.

The local chemical environment of C was studied using XPS and electron-electron coincidence measurements which were carried out at the CoESCA station [17] on the UE-52 PGM beamline [18] at the BESSY II electron storage ring. A photon energy of 420 eV was used for the measurements, and the spectra were calibrated using the Fermi edge of a clean Ag(111) crystal. The samples were cleaned using repeated cycles of argon sputtering (30 min, 500 V, 5 mA, $5{\cdot}10^{-6}$ mbar) until only a small oxygen contribution could be seen. Curve fitting was performed using the least-square fit method in the SPANCF fitting procedure of Igor Pro as presented in [19,20] with asymmetric Doniach-Sunjic line shapes used for the metallic and interstitial components, Voigt line shapes for W 5p, oxides and sp-carbon, and Shirley type background contribution. The curve fitting procedure is based on a fewest possible contribution approach where a reference sample of stoichiometric WC was used as a reference [21]. Binding energy error estimation of ±0.1 eV includes beamline calibration, spectral charge referencing, and curve fit errors unless otherwise specified.

2.3. Micromechanical testing

Free-standing cantilevers for the small-scale mechanical tests were produced by a two-step process. I) An aqueous 40 wt% KOH solution heated to ~70 °C was used to etch the Si substrates and to obtain free-standing film material. II) The cantilever geometry was machined using a Thermo Scientific Scios 2 DualBeam microscope operated at an acceleration voltage of 30 kV for the Ga^+ ion beam. A beam current of 15 nA was used for the coarse milling and 3 nA for the fine polishing. The initial notch was fabricated with 0.1 nA. The cantilevers were bent in-situ in an FEI Quanta 250 FEG scanning electron microscope with a FemtoToolsFT-NMT04 Nanomechanical Testing System. The testing rig was equipped with a diamond wedge tip, and all experiments were performed in displacement-controlled mode (10 nm s^{-1}) until failure. Eight cantilevers were tested for each sample. The critical fracture toughness (K_{IC}) is calculated as follows:

$$K_{IC} = f\left(\frac{a_0}{w}\right) * \frac{F_m l}{b w^{\frac{3}{2}}} \quad (1)$$

where F_m is the load at failure, l is the bending length from the notch to the point of force application, a_0 is the notch depth, b is the cantilever breadth, and w is the cantilever width. The cantilever dimensions were $b \approx w$ and $l \approx 7w$. The raw data for each cantilever is provided in the supplementary information Table 1. The dimensionless geometric factor $f\left(\frac{a_0}{w}\right)$ was defined, according to Matoy [22], as:

$$f\left(\frac{a_0}{w}\right) = 1.46 + 24.36\left(\frac{a_0}{w}\right) - 47.21\left(\frac{a_0}{w}\right)^2 + 75.18\left(\frac{a_0}{w}\right)^3 \quad (2)$$

The fracture surfaces were analyzed with the above-mentioned Thermo Scientific Scios 2 DualBeam microscope using an acceleration voltage of 5 kV.

3. Results and discussion

3.1. Phase analysis

Tungsten films containing 0 at.%, ~2 at.%, and ~4 at.% C were deposited by non-reactive DC magnetron sputtering from elemental targets. In the following, the samples will be named W0, W2, and W4, respectively. The GI diffraction patterns in Fig. 1 show all allowed reflections for a bcc structure, and no indications of any carbide phase are observed. The unit cell parameter of the pure W film was determined to be 3.163(3) Å, which is in good agreement with the values obtained for W films on Al_2O_3 substrates [13,14] and the literature [23]. The diffraction peaks shift towards lower 2θ angles with increasing C content, and the lattice parameter for the W4 film was determined to be 3.182(2) Å, which is also in good agreement with the values obtained in previous studies [13,14]. The increased lattice parameters and the absence of additional phases suggest the formation of a C-supersaturated solid solution. The absence of additional carbide phases was also shown by TEM analysis in ref. [13]. The θ/2θ diffraction patterns (see SI Fig. 1) show that all films exhibit a pronounced <hh0> texture which is often

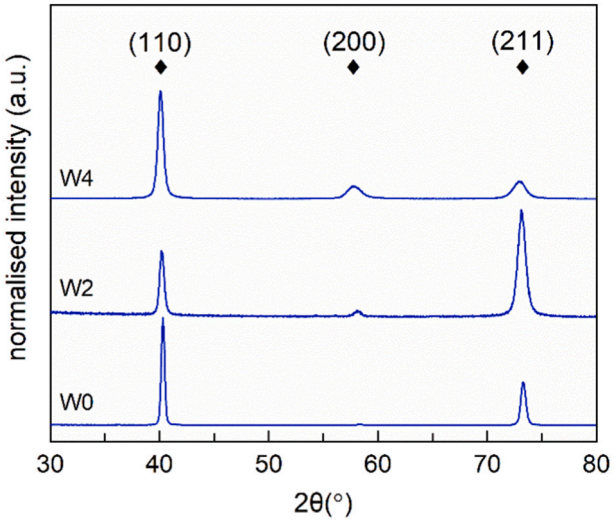

Fig. 1. GI-XRD of the W0, W2 and W4 films stacked along the y axis. The diffraction patterns are normalized to the highest intensity of the individual scan. The black triangles denote the peak position of pure W taken from ref. [13].

observed for W thin films since it is energetically most favorable for the {hh0} planes to be parallel to the substrate [24].

3.2. Atom probe tomography

The W4 film was selected for investigating the C distribution by APT since that film should be representative of all C-containing films. In Fig. 2 (a), a 3D reconstruction is presented where W and C atoms are displayed separately. The dispersion of C was found to be almost homogenous with an average content of 3.62 at.% (±0.05 at.%). The APT analysis thus confirms the formation of a supersaturated solid solution and the absence of carbide nanoclusters. The formation of such supersaturated solid solutions has previously been observed by APT for magnetron sputtered TiNbZr-O-C-N [25] and TaW-C [26] films, whereas Shinde et al. reported the formation of C nanoclusters in a CrNbTaTiW-C thin film [27]. The accuracy of C measurements by APT is sometimes limited by the performance of the detection system [28], but the composition determined by APT and the published Time-of-Flight Energy elastic recoil detection analysis (ToF-*E*-ERDA) data [13] are in good agreement. It is important to note that Ar and O (impurity elements) were detected in the APT mass spectrum with content of approximately 0.15 at.% (±0.01 at.%) each. A tomographic slice (~5 nm thick) perpendicular to the specimen axis is shown in Fig. 2 (b), which highlights a GB detected in the reconstruction, where the region exhibiting higher W atom density represents the GB. Density fluctuations of matrix elements are typically observed at GBs in APT, which stems from variations in the field evaporation threshold of the matrix elements at the lattice defects [29]. Features appearing as low-density circular areas in Fig. 2 (b) are crystallographic poles in the crystal structure (marked in grey color), which aid the identification of GBs. As seen in the atom map of C atoms in Fig. 2 (b), no clear C segregation to the GB was identified in the analysis. Nevertheless, the grain interiors and GBs can be considered relatively C-rich and O-poor since the overall C content in the material is more than twenty times higher than the O content.

3.3. X-ray photoelectron spectroscopy

The chemical environment was studied in detail using XPS, see Fig. 3, where W 4f and C 1s spectra are shown together with carbon photoelectron—Auger coincidence spectra. The most prominent W 4f peaks of the W4 sample, Fig. 3a, are assigned to metallic tungsten (W_W) with binding energies of 31.42 and 33.56 eV, close to reported values [30]. An additional contribution is observed at 32.06 and 34.20 eV (W_C), which is assigned to WC since the contribution has a similar binding

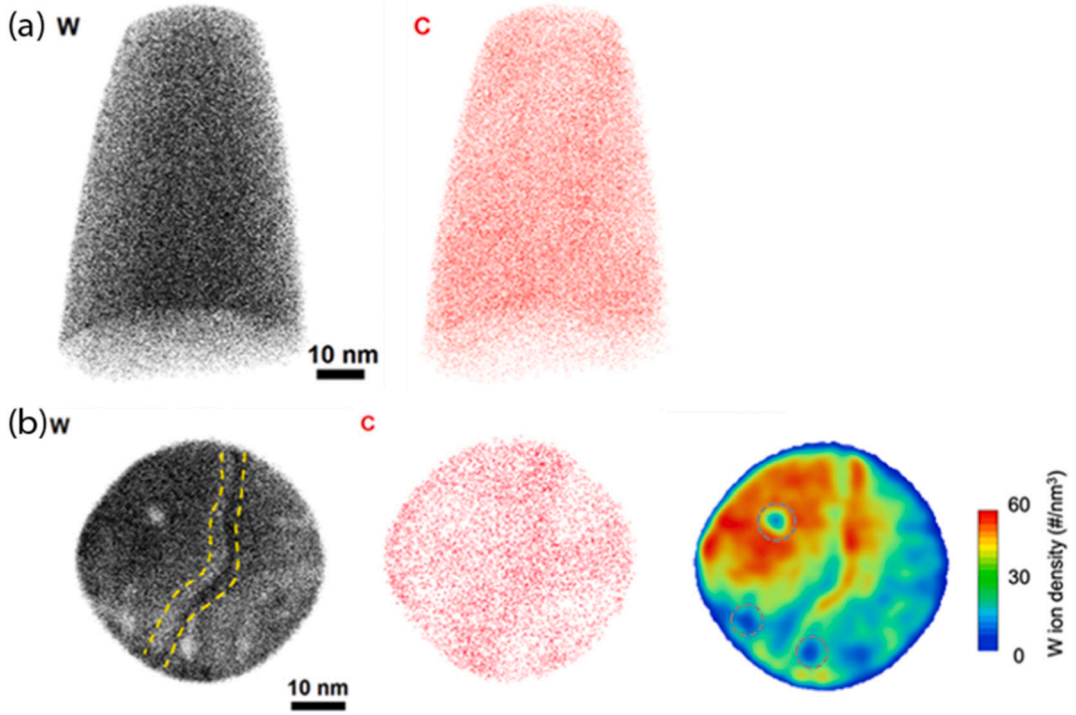

Fig. 2. (a) APT analysis of W4 showing a 3D reconstruction of the nanostructured thin film, where W and C atoms are displayed separately. (b) APT analysis showing a tomographic slice in the 3D reconstruction. (left) W atom map. The GB region is marked by yellow dotted lines. (middle) C atom map. (right) 2D density map of W atoms. Crystallographic poles are marked with grey dotted lines. (For interpretation of the references to color in this figure legend, the reader is referred to the web version of this article.)

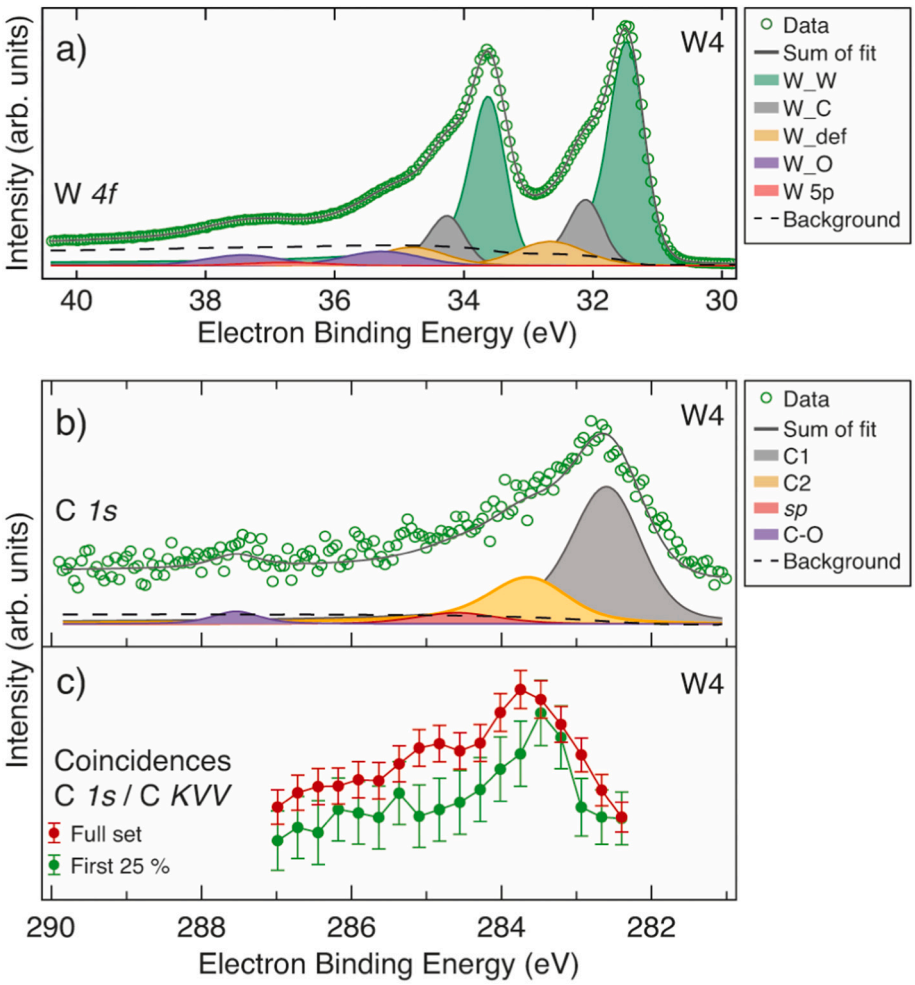

Fig. 3. a) W 4f spectra of the W4 sample recorded at 420 eV photon energy. b) C 1s XPS (top panel) and C 1s / C KVV coincidence spectra (bottom panel) of the sample, also recorded using 420 eV photon energy.

energy and a similar chemical shift to metallic tungsten as published in [31,32]. However, APT (see above) clearly shows that there is a solid solution and no carbide formation. This might seem contradictory, but we note that XPS is sensitive not to the structure, but to the electron density around a certain atom. These results therefore indicate that W has a similar chemical environment in case C is present at interstitial sites or as in a carbide. A second component at 32.65 and 34.80 eV (W_def) is believed to be a sub-stoichiometric oxide arising from Ar^+ sputtering, similar to in ref. [33]. The final contribution at higher binding energies (35.27 and 37.42 eV) is assigned to stoichiometric oxides (W_O) [33]. The W $5p_{3/2}$ line is also distinguishable at 36.8 eV.

3.4. Auger-photoelectron coincidence spectroscopy

In Fig. 3b, the C 1s XPS spectra and the C 1s spectra extracted in coincidence with C KVV Auger (Auger- Photoelectron Coincidence Spectroscopy-APECS [17]) for W4 are shown. The sample shows a main contribution in the C 1s spectrum at 282.58 eV, close to the reported value for carbidic carbon in WC [32] and in agreement with reference measurements of WC assigned similarly to W_C as interstitial C, a second component at 283.60 eV (C2), and a small contribution at 284.59 ± 0.13 eV which we assign to a mix of sp^2 and sp^3 carbon (sp) [32]. A small contribution at 287.54 ± 0.68 eV is assigned to C—O. Auger and Photoelectrons from one ionization event were measured simultaneously (APECS) to discern the carbide components further, significantly increasing the surface sensitivity [34]. The 259 to 264 eV Auger-electron energy region was selected, and the photoelectrons from those events were integrated to form the XPS coincidence spectra shown in Fig. 3c. The two spectra show the time evolution of the first 25 % (a few hours) and the complete data set (>10 h). The primary intensity seen in the coincidence spectra has similar binding energy as the C2 peak in the regular XPS, indicative that this component is on the surface of the sample. The change in the peak shape with time could come from an increase in carbon on the sample surface with time after cleaning.

3.5. Mechanical properties

Fig. 4(a) shows a representative microcantilever beam in the as-prepared state, and fracture surfaces of the W0, W2, and W4 films are presented in Fig. 4(b-d). The W0 film (Fig. 4 b) exhibits an inter-columnar fracture (crack opening and growth along the GBs) cross-section that is often associated with purely brittle fracture. The smooth fracture surface of such a fracture mode is marked by the black circle in SI Fig. 2(a)). The load-displacement curves, however, showed linear elastic behavior at the initial loading stage, followed by slight yielding before fracture (see SI Fig. 1). Inter-columnar fracture is also observed in the W2 sample (Fig. 4 c and SI Fig. 2 (b)). The fracture surface of the W4 film is much rougher than the ones of the W0 and W2 film. This is most likely caused by the fact that the columns consist of many grains. All microcantilevers of the W2 and W4 samples experienced a catastrophic failure at the maximum load and showed no signs of plastic yielding before fracture. The brittle fracture of all samples

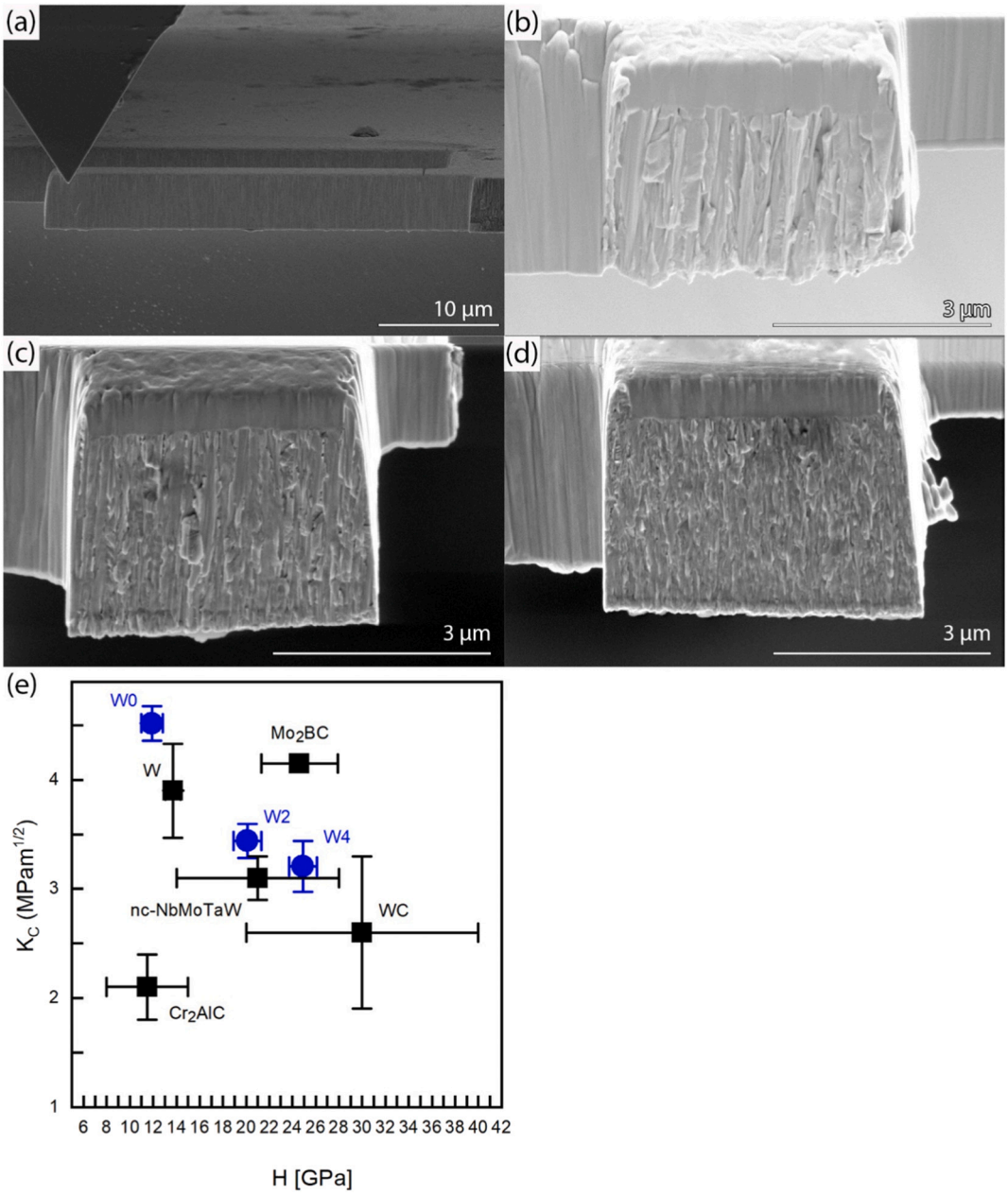

Fig. 4. (a) Representative SEM image of a microcantilever beam in the as-prepared state. Fracture cross-section of (b) W0, (c) W2 and (d) W4. (e) Ashby plot showing the critical stress intensity factor (K_C) as function of the hardness. The square black symbols show literature data for W [2], Mo_2BC [12], WC [38] and Cr_2AlC [39]. The presented values are the average with the standard deviation of the lowest and the highest reported value in the respective references.

during bending tests does not contradict the results of the micropillar compression tests since the stress states for the samples are different depending on the test type. The absence of tensile ductility in the microcantilever bending tests can be explained by a low number of GB dislocations as described in ref. [2]. Brittle fracture during cantilever tests and the absence of brittle fracture during micropillar compression test has also been reported for nc-W [2] and nc-NbMoTaW films [35,36].

Fig. 4(e) shows the K_{IC} as function of hardness in an Ashby plot format. The W0 film exhibits the highest K_{IC} with 4.52 ± 0.16 MPa·m$^{1/2}$. This must be critically assessed since signs of plasticity were observed. The determined value for W0 is of the same order of magnitude as reported in the literature for nc-W [2]. The values for the C-containing films are 3.44 ± 0.12 MPa·m$^{1/2}$ for W2 and 3.21 ± 0.24 MPa·m$^{1/2}$ for W4, around 25 % lower than the one of pure W. The critical thickness (t) must be, according to the ASTM E399, larger than $2.5\frac{K_{IC}^2}{\sigma_y^2}$, where σ_y is the yield strength. The yield strength values of the W0 and W4 samples were determined by micropillar compression tests [13], whereas the yield strength of the samples was extracted from the hardness via Tabor's constraint factor [37]. This criterion is fulfilled for the W2 and W4 films; therefore, these values can be considered to be independent of the cantilever geometry.

The results show that the addition of C can significantly increase the hardness of W films while retaining a high fracture toughness. The results also show that the W:C films exhibit similar strength-toughness properties as other novel ceramic materials that are candidates to replace traditional transition nitride and carbide materials.

4. Conclusion

In summary, we investigated the chemical distribution of up to 4 at. % C in W thin films and the influence of C content on the fracture

behavior by applying a combination of in situ micro-cantilever bending technique, APT, and XPS. The APT and XPS data show that carbon is evenly distributed in the structure, confirming the formation of a supersaturated solid solution. Additionally, the results show that the fracture toughness (~3.1 MPa·$m^{1/2}$) and hardness (~24 GPa) of W:C films can reach values almost as high as the ones of crystalline WC by microstructure modifications (grain refinement).

CRediT authorship contribution statement

S. Fritze: Writing - original draft, Conceptualization, Data curation, Formal analysis, Investigation; **R. Hahn**: Data curation, Formal analysis, Investigation, Writing - review & editing; **H Aboulfadl**: Data curation, Formal analysis, Investigation, Writing - review & editing; **F.O.L. Johansson**: Data curation, Formal analysis, Investigation, Writing - review & editing; **R. Lindblad**: Data curation, Formal analysis, Investigation, Writing - review & editing; **K. Böőr**: Data curation, Formal analysis, Investigation, Writing - review & editing; **A. Lindblad:** Funding acquisition, Project administration, Supervision, Writing - review & editing; **E. Berggren**: Data curation, Formal analysis, Investigation, Writing - review & editing; **D. Kühn**: Data curation, Formal analysis, Investigation, Writing - review & editing; **B. Osinger**: Data curation, Formal analysis, Investigation, Writing - review & editing; **T. Leitner**: Data curation, Formal analysis, Investigation, Writing - review & editing; **E. Lewin**: Data curation, Formal analysis, Investigation, Writing - review & editing; **U. Jansson:** Funding acquisition, Project administration, Supervision, Writing - review & editing; **P.H. Mayrhofer:** Funding acquisition, Project administration, Supervision, Writing - review & editing; **M. Thuvander:** Funding acquisition, Project administration, Supervision, Writing - review & editing;

Declaration of competing interest

The authors declare that they have no known competing financial interests or personal relationships that could have appeared to influence the work reported in this paper.

Data availability

The data that support the findings of this study are available from the corresponding author upon reasonable request.

Acknowledgments

Stefan Fritze thanks Teresa Fritze and Ariadna Lara Gutierrez for their assistance with the figures. We thank the Helmholtz-Zentrum Berlin für Materialien und Energie for the allocation of synchrotron radiation beamtime. Technical support by HZB staff at BESSY II during experiment at the CoESCA endstation (UE52_PGM) as well as surface preparation at the Low-Dose PES endstation (PM4) is gratefully acknowledged. K.B acknowledges the Swedish Foundation for Strategic Research (contract RMA15-0048) and AB Sandvik Coromant. The APT work was performed at Chalmers Materials Laboratory (CMAL). The authors acknowledge the use of the USTEM facility at TU Wien.

Appendix A. Supplementary data

Supplementary data to this article can be found online at https://doi.org/10.1016/j.surfcoat.2023.130326.

References

[1] K.S. Kumar, H. Van Swygenhoven, S. Suresh, Mechanical behavior of nanocrystalline metals and alloys, Acta Mater. 51 (2003) 5743–5774, https://doi.org/10.1016/j.actamat.2003.08.032.

[2] O. El-Atwani, J. Gigax, M. Chancey, J.K.S. Baldwin, S.A. Maloy, Nanomechanical properties of pristine and heavy ion irradiated nanocrystalline tungsten, Scr. Mater. 166 (2019) 159–163, https://doi.org/10.1016/j.scriptamat.2019.03.014.

[3] A. Leitner, V. Maier-Kiener, D. Kiener, Extraction of flow behavior and Hall–Petch parameters using a nanoindentation multiple sharp tip approach, Adv. Eng. Mater. 19 (2017) 1–9, https://doi.org/10.1002/adem.201600669.

[4] A. Joshi, D.F. Stein, Intergranular brittleness studies in tungsten using auger spectroscopy, Metallurgical Transactions 1 (1970) 2543–2546, https://doi.org/10.1007/BF03038381.

[5] C. Tian, Y. Ma, A. Ghafarollahi, P. Patil, G. Dehm, E. Bitzek, M. Rasinski, J.P. Best, Segregation-enhanced grain boundary embrittlement of recrystallised tungsten evidenced by site-specific microcantilever fracture, Acta Mater. 259 (2023), 119256, https://doi.org/10.1016/j.actamat.2023.119256.

[6] M. Wurmshuber, S. Jakob, S. Doppermann, S. Wurster, R. Bodlos, L. Romaner, V. Maier-Kiener, D. Kiener, Tuning mechanical properties of ultrafine-grained tungsten by manipulating grain boundary chemistry, Acta Mater. 232 (2022), 117939, https://doi.org/10.1016/j.actamat.2022.117939.

[7] D. Scheiber, R. Pippan, P. Puschnig, L. Romaner, Ab initio search for cohesion-enhancing impurity elements at grain boundaries in molybdenum and tungsten, Model. Simul. Mater. Sci. Eng. 24 (2016), https://doi.org/10.1088/0965-0393/24/8/085009.

[8] S. Fritze, P. Malinovskis, L. Riekehr, L. von Fieandt, E. Lewin, U. Jansson, Hard and crack resistant carbon supersaturated refractory nanostructured multicomponent coatings, Sci. Rep. 8 (2018) 14508, https://doi.org/10.1038/s41598-018-32932-y.

[9] G. Greczynski, J. Lu, O. Tengstrand, I. Petrov, J.E. Greene, L. Hultman, Nitrogen-doped bcc-Cr films: combining ceramic hardness with metallic toughness and conductivity, Scr. Mater. 122 (2016) 40–44, https://doi.org/10.1016/j.scriptamat.2016.05.011.

[10] L. Yang, K. Zhang, M. Wen, Z. Hou, C. Gong, X. Liu, C. Hu, X. Cui, W. Zheng, Highly hard yet toughened bcc-W coating by doping unexpectedly low B content, Sci. Rep. 7 (2017) 1–8, https://doi.org/10.1038/s41598-017-09807-9.

[11] L. Yang, C. Liu, M. Wen, X. Dai, Y. Zhang, X. Chen, K. Zhang, Small atoms as reinforced agent for both hardness and toughness of group-VIB transition metal films, J. Alloys Compd. 735 (2018) 1105–1110, https://doi.org/10.1016/j.jallcom.2017.11.208.

[12] R. Soler, S. Gleich, C. Kirchlechner, C. Scheu, J.M. Schneider, G. Dehm, Fracture toughness of Mo2BC thin films: intrinsic toughness versus system toughening, Materials and Design. 154 (2018) 20–27, https://doi.org/10.1016/j.matdes.2018.05.015.

[13] S. Fritze, M. Chen, L. Riekehr, B. Osinger, M.A. Sortica, A. Srinath, A.S. Menon, E. Lewin, D. Primetzhofer, J.M. Wheeler, U. Jansson, Magnetron sputtering of carbon supersaturated tungsten films – a chemical approach to increase strength, Mater. Des. 208 (2021), 109874, https://doi.org/10.1016/j.matdes.2021.109874.

[14] B.O. Mukhamedov, S. Fritze, M. Ottosson, B. Osinger, E. Lewin, B. Alling, U. Jansson, I.A. Abrikosov, Tetragonal distortion in magnetron sputtered bcc-W films with supersaturated carbon, Materials and Design. 214 (2022), 110422, https://doi.org/10.1016/j.matdes.2022.110422.

[15] E.A. Marquis, M. Bachhav, Y. Chen, Y. Dong, L.M. Gordon, A. McFarland, On the current role of atom probe tomography in materials characterization and materials science, Curr. Opinion Solid State Mater. Sci. 17 (2013) 217–223, https://doi.org/10.1016/j.cossms.2013.09.003.

[16] K. Thompson, D. Lawrence, D.J. Larson, J.D. Olson, T.F. Kelly, B. Gorman, In situ site-specific specimen preparation for atom probe tomography, Ultramicroscopy 107 (2007) 131–139, https://doi.org/10.1016/j.ultramic.2006.06.008.

[17] T. Leitner, A. Born, I. Bidermane, R. Ovsyannikov, F.O.L. Johansson, Y. Sassa, A. Föhlisch, A. Lindblad, F.O. Schumann, S. Svensson, N. Mårtensson, The CoESCA station at BESSY: auger electron–photoelectron coincidences from surfaces demonstrated for ag MNN, J. Electron Spectrosc. Relat. Phenom. 250 (2021), 147075, https://doi.org/10.1016/j.elspec.2021.147075.

[18] D.R. Batchelor, Th. Schmidt, R. Follath, C. Jung, R. Fink, M. Knupfer, A. Schöll, T. Noll, F. Siewert, B. Büchner, E. Umbach, An energy-dispersive VUV beamline for NEXAFS and other CFS/CIS studies, Nucl. Instrum. Methods Phys. Res., Sect. A 575 (2007) 470–475, https://doi.org/10.1016/j.nima.2007.02.108.

[19] E. Kukk, K. Ueda, U. Hergenhahn, X.-J. Liu, G. Prümper, H. Yoshida, Y. Tamenori, C. Makochekanwa, T. Tanaka, M. Kitajima, H. Tanaka, Violation of the Franck-Condon principle due to recoil effects in high energy molecular Core-level photoionization, Phys. Rev. Lett. 95 (2005), 133001, https://doi.org/10.1103/PhysRevLett.95.133001.

[20] E. Kukk, G. Snell, J.D. Bozek, W.-T. Cheng, N. Berrah, Vibrational structure and partial rates of resonant auger decay of the N 1 s → 2 π core excitations in nitric oxide, Phys. Rev. A 63 (2001), 062702, https://doi.org/10.1103/PhysRevA.63.062702.

[21] K. Böőr, Chemical vapor deposition of hard coatings: Development of W(C,N) coatings for cemented carbide and TiN deposition on a CoCrFeNi substrate, Acta Universitatis Upsaliensis, n.d. urn:nbn:se:uu:diva-487198.

[22] K. Matoy, H. Schönherr, T. Detzel, T. Schöberl, R. Pippan, C. Motz, G. Dehm, A comparative micro-cantilever study of the mechanical behavior of silicon based passivation films, Thin Solid Films 518 (2009) 247–256, https://doi.org/10.1016/j.tsf.2009.07.143.

[23] H.E. Swanson, E. Tatge, Standard X-ray diffraction powder patterns, NBS Circular 359 (1953) 28–29.

[24] F.T.N. Vüllers, R. Spolenak, Alpha- vs. beta-W nanocrystalline thin films: a comprehensive study of sputter parameters and resulting materials' properties, Thin Solid Films 577 (2015) 26–34, https://doi.org/10.1016/j.tsf.2015.01.030.

[25] C. Liu, W. Lu, W. Xia, C. Du, Z. Rao, J.P. Best, S. Brinckmann, J. Lu, B. Gault, G. Dehm, G. Wu, Z. Li, D. Raabe, Massive interstitial solid solution alloys achieve

near-theoretical strength, Nature Communications 13 (2022) 1–9, https://doi.org/10.1038/s41467-022-28706-w.
[26] S. Fritze, M. Hans, L. Riekehr, B. Osinger, E. Lewin, J.M. Schneider, U. Jansson, Influence of carbon on microstructure and mechanical properties of magnetron sputtered TaW coatings, Mater. Des. 196 (2020), 109070, https://doi.org/10.1016/j.matdes.2020.109070.
[27] D. Shinde, S. Fritze, M. Thuvander, P. Malinovskis, L. Riekehr, U. Jansson, K. Stiller, Elemental distribution in CrNbTaTiW-C high entropy alloy thin films, Microsc. Microanal. 25 (2019) 489–500, https://doi.org/10.1017/S1431927618016264.
[28] M. Thuvander, D. Shinde, A. Rehan, S. Ejnermark, K. Stiller, Improving compositional accuracy in APT analysis of carbides using a decreased detection efficiency, Microsc. Microanal. 25 (2019) 454–461, https://doi.org/10.1017/S1431927619000424.
[29] C. Oberdorfer, S.M. Eich, G. Schmitz, A full-scale simulation approach for atom probe tomography, Ultramicroscopy 128 (2013) 55–67, https://doi.org/10.1016/j.ultramic.2013.01.005.
[30] C. Kalha, L.E. Ratcliff, J.J.G. Moreno, S. Mohr, M. Mantsinen, N.K. Fernando, P. K. Thakur, T.-L. Lee, H.-H. Tseng, T.S. Nunney, J.M. Kahk, J. Lischner, A. Regoutz, Lifetime effects and satellites in the photoelectron spectrum of tungsten metal, Phys. Rev. B 105 (2022), 045129, https://doi.org/10.1103/PhysRevB.105.045129.
[31] J. Luthin, C. Linsmeier, Carbon films and carbide formation on tungsten, Surf. Sci. 454–456 (2000) 78–82, https://doi.org/10.1016/S0039-6028(00)00181-3.
[32] P.V. Krasovskii, O.S. Malinovskaya, A.V. Samokhin, Y.V. Blagoveshchenskiy, V. A. Kazakov, A.A. Ashmarin, XPS study of surface chemistry of tungsten carbides nanopowders produced through DC thermal plasma/hydrogen annealing process, Appl. Surf. Sci. 339 (2015) 46–54, https://doi.org/10.1016/j.apsusc.2015.02.152.
[33] A. Katrib, F. Hemming, P. Wehrer, L. Hilaire, G. Maire, The multi-structure of oxidized-reduced tungsten carbide surface(s), Catal. Lett. 29 (1994) 397–408, https://doi.org/10.1007/BF00807119.
[34] A. Born, F.O.L. Johansson, T. Leitner, D. Kühn, A. Lindblad, N. Mårtensson, A. Föhlisch, Separation of surface oxide from bulk Ni by selective Ni 3p photoelectron spectroscopy for chemical analysis in coincidence with Ni M-edge auger electrons, Sci. Rep. 11 (2021) 16596, https://doi.org/10.1038/s41598-021-96108-x.
[35] Y. Zou, H. Ma, R. Spolenak, Ultrastrong ductile and stable high-entropy alloys at small scales, Nat. Commun. 6 (2015) 7748, https://doi.org/10.1038/ncomms8748.
[36] Y. Xiao, Y. Zou, H. Ma, A.S. Sologubenko, X. Maeder, R. Spolenak, J.M. Wheeler, Nanostructured NbMoTaW high entropy alloy thin films: high strength and enhanced fracture toughness, Scr. Mater. 168 (2019) 51–55, https://doi.org/10.1016/j.scriptamat.2019.04.011.
[37] D. Tabor, The hardness and strength of metals, J. Inst. Met. 79 (1951) 1–18.
[38] T. Glechner, R. Hahn, L. Zauner, S. Rißlegger, A. Kirnbauer, P. Polcik, H. Riedl, Structure and mechanical properties of reactive and non-reactive sputter deposited WC based coatings, J. Alloys Compd. 885 (2021), 161129, https://doi.org/10.1016/j.jallcom.2021.161129.
[39] B. Völker, B. Stelzer, S. Mráz, H. Rueß, R. Sahu, C. Kirchlechner, G. Dehm, J. M. Schneider, On the fracture behavior of Cr2AlC coatings, Materials and Design. 206 (2021), https://doi.org/10.1016/j.matdes.2021.109757.